applied optics

All-fiber probes for endoscopic optical coherence tomography of the large airways

Santosh Balakrishnan[1] [ID] and Amy L. Oldenburg[1,2,3,*]

[1]*Department of Biomedical Engineering, University of North Carolina at Chapel Hill, Chapel Hill, North Carolina 27599, USA*
[2]*Department of Physics and Astronomy, University of North Carolina at Chapel Hill, Chapel Hill, North Carolina 27599, USA*
[3]*University of North Carolina at Chapel Hill, Biomedical Research Imaging Center, Chapel Hill, North Carolina 27599, USA*
*Corresponding author: aold@physics.unc.edu

Endoscopic optical coherence tomography of large airways poses unique challenges. A hybrid lens is described that consists of a section of coreless fiber and graded index fiber (GIF), followed by a ball lens section. This design produces low numerical aperture beams better suited for large airway imaging. The performance of this lens is compared against conventional GIF and ball lens designs. Forward- and side-viewing probes were modeled, fabricated, and tested. The impact of a sheath on the beam profile was also investigated. Probes with working distances larger than 10 mm and depth-of-focus exceeding 12 mm are demonstrated with the proposed design.   © 2021 Optical Society of America under the terms of the OSA Open Access Publishing Agreement

https://doi.org/10.1364/AO.431010

1. INTRODUCTION

Endoscopic optical coherence tomography (OCT) systems equipped with single-mode fiber-optic probes have been shown to be valuable in a wide range of clinical applications [1,2]. Endoscopic OCT imaging of the nasal cavity, the upper airway, the trachea, and the mainstem bronchi is a promising approach for the diagnosis and monitoring of conditions like nasal valve compromise [3], obstructive sleep apnea [4,5], subglottic stenosis [6] and central airway obstruction [7]. Unlike other endoscopic OCT applications, such as intravascular or esophageal imaging, large airway imaging is particularly challenging owing to the large size of the organs being imaged and the inability to center the probe within the lumen using a balloon catheter or capsule [2], which would relax requirements on the depth of focus (DoF). Owing to these considerations, probes designed for large airway OCT imaging usually utilize a side-looking, low numerical aperture (NA) beam with working distances (WDs) typically greater than 10 mm. To achieve such a beam profile, a probe design consisting of a bulk gradient refractive index (GRIN) lens and a glass spacer, combined with a prism to deflect the beam, has been most commonly employed [4,5].

Probe designs based on bulk glass components, such as GRIN lenses and glass rods, are very versatile and have been widely employed in a range of endoscopic OCT applications [2]. However, GRIN lens-based probe elements need to be carefully aligned and fixed in a manner that allows their alignment to remain unaffected as the probe rotates [8,9]. A correctly aligned assembly is typically achieved with some form of housing, which in turn results in a rigid distal end. Such rigid tips could make such probes difficult to introduce into sections with tight bends,

such as the working port of a flexible bronchoscope or a tortuous luminal organ. The refractive index mismatches at the interfaces between the elements also result in losses [9,10]. Additionally, the end faces of the various elements need to be angle-polished to avoid Fresnel reflections from the interfaces from being coupled back into the imaging system [2].

An alternative to utilizing bulk glass elements is to use only fiber-optic components to form the lens at the tip of the OCT probe. Such all-fiber lenses are constructed using fusion-spliced segments, which ensures that the lens segments are correctly aligned, with extremely low-loss interfaces. Such designs also feature fused elements that are more mechanically robust than probes formed with bulk glass elements glued together. All-fiber probes are better suited for applications that require miniature, flexible probes owing to the smaller dimensions of fiber-optic elements and the lack of any rigid elements at the probe tip [2]. A wide range of all-fiber lens designs, based on ball lenses [11–13], graded index fibers (GIFs) [14–16] or other elements [14,17,18], have been described in the literature. However, such designs typically produce imaging beams with short WDs—typically less than 3 mm, making such probes better suited for imaging small luminal organs [19,20] or for applications where the tissue is in contact with the probe [21,22].

In this paper, the design of all-fiber probes suitable for endoscopic OCT imaging of large luminal organs is systematically analyzed. In particular, the design and fabrication of all-fiber lenses that generate low NA beams is discussed. Such beams are better suited for applications where the distance between the probe and the tissue surface is unknown and variable [23]. Three types of all-fiber lenses were designed and fabricated using

standard, off-the-shelf, 125 µm fibers. The first type of design examined was the combination of coreless fiber (CF) spacer with a GIF. The ball lens probe, formed by splicing a segment of CF and melting the CF tip to form a ball, was considered next, Finally, a novel, hybrid design that used a combination of the first two designs was analyzed. The hybrid design utilizes an initial segment of CF spacer and GIF to compress the beam emerging from the single-mode fiber (SMF). A subsequent section consisting of another CF spacer with a ball lens tip focuses the beam.

The lenses were modeled using ABCD transfer matrices, and their beam profiles were predicted using Gaussian beam propagation. Several probes, based on each type of design, were fabricated, and their beam profiles were measured and compared against the predicted results. Only forward-viewing designs of the GIF-based lens were examined, while angle polishing of the ball tip was used to obtain side-viewing beams for the ball lens and the hybrid designs. Finally, the impact of enclosing the angle-polished, hybrid probe in a sheath was investigated by comparing the measured beam profiles and OCT images acquired with and without the sheath.

2. THEORY

A. ABCD Models and Beam Parameters

The fiber lenses were modeled as paraxial optical systems using the ABCD matrix method. The GIF lens, ball lens, and the hybrid lens design schematics are shown in Figs. 1(a)–1(b). In the figure, n_f denotes the SMF core refractive index, the CF sections have a refractive index of n_s, l_{s1} or l_{s2} is the length of the CF segment, the radius of the spherical tip is r_b, n_g is the refractive index along the central axis of the GIF, g is the gradient factor of the GIF, and l_g is the length of the GIF section. The length of the straight segment of the CF spacer in Figs. 1(b) and 1(c), l_s, is given by $l_s = l_{s2} - 2r_b$.
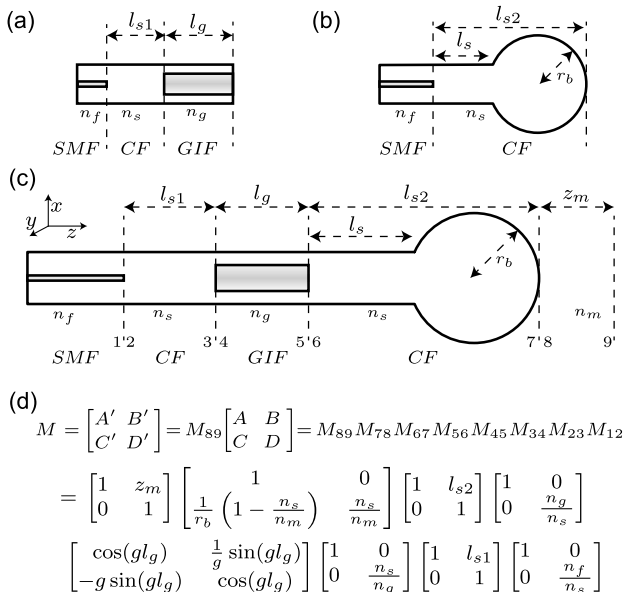
Fig. 1. All-fiber lens designs. (a) GIF-based lens; (b) ball lens; (c) hybrid lens with a combination of a CF-GIF segment and a ball lens segment; (d) common ABCD model for either forward- or side-viewing hybrid lens.

The ABCD model for the hybrid lens is given in Fig. 1(d). The ball lens model may be obtained by setting $g = 1$ and $l_g = l_{s1} = 0$. Similarly, the ABCD model for the GIF lens may be obtained by setting $r_b = \infty$ and $l_{s2} = 0$. A side-viewing probe, based on either the ball lens or the hybrid lens design, is usually obtained by angle polishing half of the spherical tip and utilizing either total internal reflection or a metal coating of the polished face to redirect the beam. Therefore, the ABCD models for both forward- and side-viewing variants of such lenses are identical. Only forward-viewing GIF probe designs, as shown in Fig. 1(a), are considered here.

The ABCD models, along with the Gaussian beam propagation, using the complex q-parameter, can be used to determine expressions for the WD (the distance between the probe exit surface and the beam waist), the spot size (SS, twice the beam radius at the waist), and the beam diameter (BD) versus distance from the probe tip z_m in a homogeneous output medium [8,24–26],

$$WD = -\frac{BD + ACn_f^2 z_R^2}{D^2 + C^2 n_f^2 z_R^2}, \tag{1}$$

$$SS = 2\left[\frac{\lambda_0 n_f^2 z_R}{\pi n_m^2}\left(\frac{1}{D^2 + C^2 n_f^2 z_R^2}\right)\right]^{1/2}, \tag{2}$$

$$BD(z_m) = 2\left[\frac{\lambda_0}{\pi n_f^2 z_R}\left(A'^2 n_f^2 z_R^2 + B'^2\right)\right]^{1/2}. \tag{3}$$

In the expressions above, λ_0 is the wavelength of light in free space, z_R is the Rayleigh range given by $z_R = \pi w_{0f}^2/\lambda_0$ with w_{0f} being half the mode field diameter (MFD) of the SMF at λ_0, and n_m is the refractive index of the output medium. A, B, C, and D are elements of the ABCD model, where the output plane is assumed to be at the probe exit surface and A', B', C', and D' are elements of the ABCD model when the output plane is situated at distance z_m from the probe exit surface in the output medium ($A' = A + Cz_m$, $B' = B + Dz_m$, $C' = C$ and, $D' = D$). The input plane is set to be at the tip of the SMF, where the Gaussian beam is assumed to have its waist. Analytical expressions for WD and SS for each lens type may be obtained by computing the values of A, B, C, and D by multiplying the matrices together and then by substitution in Eqs. (1) and (2). The resulting expressions are independent of n_f.

B. Predicted Beam Profiles

The GIF-based lens design consists of a segment of CF (l_{s1}) spliced to the SMF that acts as a beam expander, followed by a length of GIF (l_g) that functions as a lens to focus the beam. In principle, the lengths of the CF and GIF segments may be tuned to obtain a range of output beam profiles in a method similar to that used with bulk GRIN lens designs [25]. However, such probes, when fabricated from commercially available GIFs [10,16,27], typically produce beams with a short WD and a rapidly diverging profile that are not ideal for large airway imaging. However, by appropriate selection of the segment lengths, the CF-GIF segment can be used to produce a beam with a waist at the GIF tip and a SS smaller than the MFD of the SMF. As will

be shown below, the compressed SS offered by such a choice is favorable as a first stage in the hybrid lens design.

The relationship between the probe segment lengths and the resulting beam profiles for GIF lens designs are visualized as contour plots of WD and SS, shown in Figs. 2(a) and 2(b), respectively. The pitch of the GIF segment, $p_g = g l_g / (2\pi)$, is used instead of l_g due to the periodic nature of the beam trajectory in the GIF core. The maximum length of the spacer segment, l_{s1}, is set to limit the beam to the GIF core. Probe designs along the dashed curve in Fig. 2(a) yield the largest possible WD, while probe designs along the dashed curve in Fig. 2(b) result in the longest DoF (defined to be twice the Rayleigh range), which scales with SS according to Gaussian beam theory. While in general, a small SS is desirable to preserve imaging resolution, here we prefer a large SS, as DoF tends to be a limiting factor in large airway imaging. The dashed-dotted curve in Fig. 2(b) is the contour of the minimum SS, and selecting CF and GIF lengths that lie along this curve would result in probes that yield the smallest SSs.

Similar plots for the ball lens and the hybrid lens are shown in Figs. 2(c)–(f). The maximum spacer length, l_s, for both designs, is set to ensure that the BD does not exceed the CF diameter. For the hybrid lens, l_{s1} and l_g are kept fixed at 272 and 326 μm, respectively, to obtain an input BD of ~ 4.4 μm at the input face of the second CF segment (this is the smallest BD achievable with the fibers described in the Methods section, while ensuring that the GIF core fill factor is less than $2/\pi$ [27]). The dashed curves again indicate the contours of the maximum WD or the maximum SS. Note that an SMF-GIF section alone cannot produce a beam with a waist size smaller than the MFD of the SMF [16,24].

The contours of the maximum WD and maximum SS for all the designs are parallel to each other. Additionally, the contours for the ball lens and the hybrid lens designs have the same slope, but different offsets. In particular, it can be noted that the function of the CF-GIF segment in the hybrid design is to increase

the WDs achievable with similar l_s and r_b values, but at the cost of larger SSs. The expressions for these contours can be found in Ref. [28].

The maximum predicted WD, with the segment lengths shown in Fig. 2, for the GIF lens, the ball lens, and the hybrid lens, is ~ 1.2 mm, ~ 5 mm and ~ 19.5 mm, respectively. The probe designs that were selected to be fabricated and tested are indicated by the diamond markers on the plots.

C. Angle Polishing

Endoscopic imaging of luminal organs, such as the airway, is best accomplished using a beam that emerges nearly perpendicular to the axis of the probe, i.e., a side-viewing beam. In order to determine the optimal polishing angle, consider Fig. 3, which depicts a Gaussian beam originating at its waist in the CF and being incident on an interface between the CF and the medium that is polished at an angle α. Total internal reflection occurs if the beam incidence angle is greater than the critical angle $\theta_c = \sin^{-1}(n_m / n_s)$. While the angle of incidence for a ray along the central axis is α, the angle of incidence for the portions of the beam above the axis is less than α. If the distance between the beam waist and polished surface is much larger than the Rayleigh range, then the divergence of the beam may be characterized using the angle $\theta = \lambda_0 / (\pi w_0 n_s)$. Thus, in order for all portions of the beam to satisfy the total internal reflection condition, $\alpha - \theta > \theta_c$ or,

$$\alpha > \sin^{-1}\left(\frac{n_m}{n_s}\right) + \frac{\lambda_0}{\pi w_0 n_s}. \tag{4}$$

After reflection, the OCT beam emerges from the probe at an angle $\beta = 2(\alpha - \pi/4)$ relative to the plane perpendicular to the fiber axis. For this side-viewing beam, the z axis is considered to be in the direction of propagation, the x axis is considered to be along the length of the probe, and the y axis is considered to be perpendicular to the probe axis.
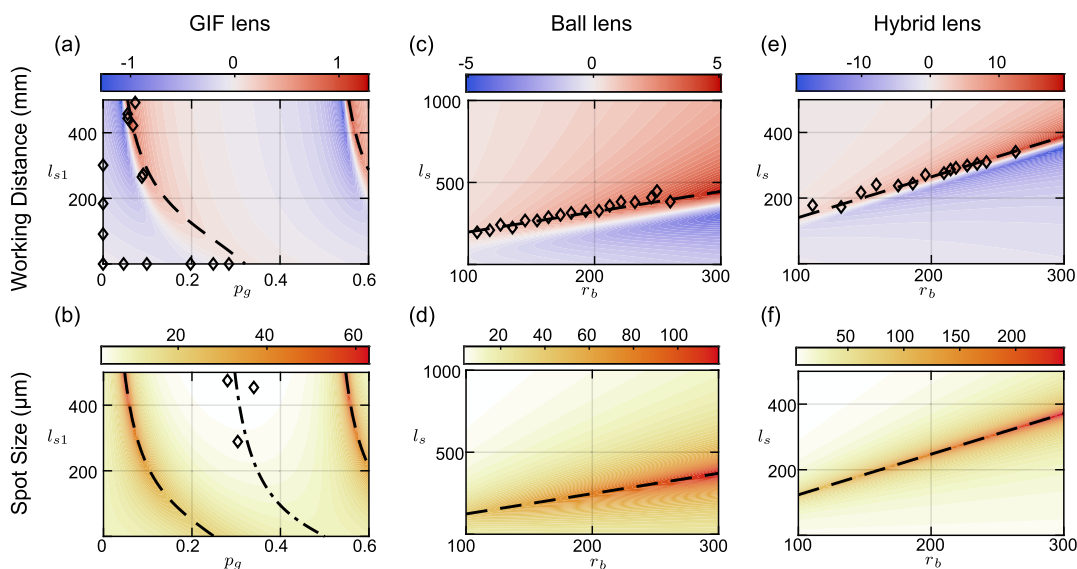
Fig. 2. Contour plots of the WD and SS. (a) GIF-based lens WD; (b) GIF-based lens SS; (c) ball lens WD; (d) ball lens SS; (e) hybrid lens WD; (f) hybrid lens SS. Dashed lines indicate the contours of the maximum values; dashed-dotted line in (b) indicates the minimum SS contour. Diamond markers depict some of the lens designs fabricated and tested. p_g, GIF pitch; l_{s1}, l_s, spacer lengths in micrometers; r_b, ball radius in micrometers.
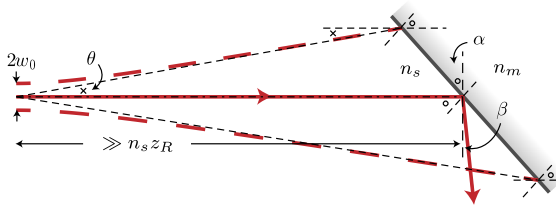
Fig. 3. Gaussian beam incident on an angle-polished interface.

Additionally, endoscopic OCT imaging is always performed with the probe enclosed in a sheath, which may be characterized by its internal diameter, $2r_h$, the wall thickness, t_h, and the refractive index of the material, n_h. The sheath can be modeled using different ABCD matrices for each orthogonal direction [25,26]. Due to the cylindrical shape of the sheath, in the x direction, the waist location is shifted farther by $t_h(n_h - n_m)/n_h$ and the SS remains the same. However, when using the sheath described in the Methods section, the beam is expected to lose its focus in the y direction.

3. METHODS

The all-fiber probes were designed to be compatible with an endoscopic OCT system suitable for airway imaging and operating at a central wavelength of 1.3 µm [23]. The OCT system uses standard SMF-28 fiber with a 125 µm cladding and 9.2 µm MFD at 1.3 µm (SMF-28, Thorlabs Inc.) for its sample and reference arms. Therefore, the beam radius at the tip of the SMF is modeled to be $w_{0f} = 9.2/2$ and $n_f = 1.0036 n_{silica}$, where $n_{silica} = 1.4469$ is the refractive index of silica at 1.3 µm. The GIF has a 62.5 µm core and 125 µm cladding (GIF625, Thorlabs Inc.), and the fiber parameters $g = 6.336 \times 10^{-3}$ µm^{-1}, $n_g = 1.4761$ [27] were found to yield ABCD predictions that matched reasonably well with the measurements. The CF has a diameter of 125 µm and is made of pure silica (FG125LA, Thorlabs Inc.); therefore, $n_s = n_{silica}, n_s = n_{silica}$. Measurements with the sheath were made using a fluorinated ethylene propylene (FEP) sheath with inner/outer diameter of 540/840 µm and nominal refractive index of $n_h = 1.34$.

A Vytran FFS2000 fiber workstation (Thorlabs Inc.) was used to strip, cleave, and fusion-splice different elements of the fiber probes. A dedicated ball lensing system, 3SAE BLS (3SAE Technologies Inc.), was used to melt the fiber and form spherical tips [29]. In order to form a spherical tip, the cleaved fiber tip was positioned below the electrodes and a short (~ 3s) arc discharge was performed. The diameter of the resulting spherical tip was measured, and the arc discharge was repeated after moving the fiber tip back to the starting position to increase the ball size. These steps were repeated manually until the desired ball diameter was obtained. Smaller adjustments to the ball diameter were performed by positioning the tip farther away from the electrodes.

In order to angle-polish the spherical tip, the probe was mounted on a dedicated fiber holder with an angled ferrule at its tip. Crystalbond 509 (Ted Pella Inc.) adhesive polymer was used to mount the ball-tipped fiber on the ferrule. The polishing angle was estimated using Eq. (4), assuming the wavelength to

be 1.36 µm (the longest wavelength for a swept laser source with a sweep range of ~ 120 nm [23]). For the ball lens design, the polishing angle relation was found to be $\alpha > 47.5°$, assuming $w_0 = 9.2/2$ µm. For the hybrid lens, the relation was $\alpha > 51.9°$, assuming $w_0 = 4.2/2$ µm after the CF-GIF segment. Thus, the polishing angle was chosen to be 48° for ball lens probes and 52° for hybrid lens probes. These polishing angles provide a beam exit angle of 6° or 14°, respectively.

Angle polishing was performed using the Ultrapol Polishing system (Ultratec Manufacturing Inc.); 50% of the spherical tip was polished in stages under a slow, steady trickle of water. First, a 6 µm diamond film was used to remove most of the glass, followed by polishing with 1 and 0.5 µm diamond lapping films to obtain a smooth polished surface. After polishing, the probe was unmounted by dissolving the polymer in acetone, and then cleaned by immersing in acetone, followed by an ultrasonic isopropyl bath. The high magnification imaging of the FFS2000 workstation was used to acquire images of the probes at various stages of the fabrication process. The workstation's imaging system has a field of view of 480×360 µm and the saved images were 1032×776 pixels; therefore, a constant factor of 2.15 was used to convert measurements in pixels to micrometers. Multiple images were acquired and stitched based on landmarks to assemble the full probe images, shown in the Results section. The stitched images were used to measure the dimensions of the various probe elements. The linear dimensions were measured using straight lines between visible fiber features such as splice joints or the SMF core tip, and the diameter of the spherical tip was measured by manually drawing a best-fitting circle.

Beam profiles were measured with the Nanoscan Ge/9/5 µm (Ophir-Spiricon LLC.) scanning slit beam profiler. The measured BDs were compared against the ABCD predicted beam profile using the root mean square error (RMSE) metric. The measured BDs in the x and y directions are denoted by BD_x and BD_y in the Results section. A comparison of predicted and measured beam profiles from some initial ball lens probes showed that the measurement method of using the best-fit circle
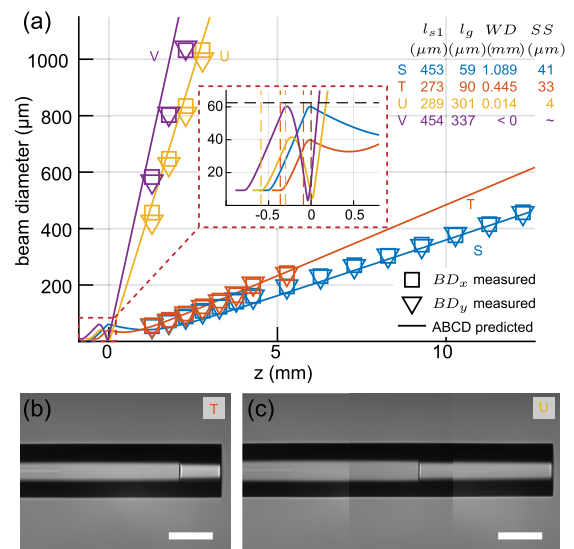

Fig. 4. GIF lens results. (a) Measured and predicted beam profiles; (b) image of the probe marked T; (c) image of the probe U; scale bars are 100 µm.

overestimated r_b by ~ 5 µm. Therefore, for ball lens probes, the measured value of r_b was reduced by 5 µm, and the measured value of l_s was increased by 10 µm, such that the overall length of the CF segment (l_{s2}) retained its measured value. The ABCD predictions for ball lens probes were also compared against results obtained from OpticStudio (Zemax LLC.); the results of this comparison are presented in the Supplement 1. For the hybrid lenses, the measured value of r_b was reduced by 10 µm, and the measured value of l_s was increased by 20 µm. The reported values of l_s and r_b in the Results section, for both the designs, are after these corrections. The ABCD predicted beam profiles, used for comparison with the measured BDs, were also obtained with ABCD models that used the corrected lengths of l_s and r_b for both designs.

OCT images were acquired with a cart-based swept source OCT system with a center wavelength of 1300 nm, A-line rate of 100 kHz, axial resolution of ~ 13 µm, peak sensitivity of ~ 106 dB, and an imaging range of 12 mm [23]. Images were acquired in a rolled paper cylinder with a printed pattern of alternating black and white, 125 µm, lines, and in an excised pig trachea.

4. RESULTS

Representative results for forward-viewing GIF lenses are shown in Fig. 4. The measured and predicted beam profiles for two sets of lenses are shown in Fig. 4(a). The inset shows an enlarged view of the predicted beam profile within the lens segments. The table shown on the figure summarizes the lens segment lengths along with the predicted WD and SS.

Probes with profiles marked as S and T were designed to achieve the maximum possible WD, while the probe segment lengths for probes U and V were chosen to obtain a compressed SS at the GIF tip. Figures 4(b) and 4(c) show images of the probes that produced plots T and U, respectively. The inset in Fig. 4(a) indicates that the beam waist locations for probes U

and V are very close to the probe tip and that the waist sizes are less than the MFD of the SMF.

Probe S achieved a WD of ~ 1.1 mm with a GIF fill factor of 96.3%, while probe T had a WD of ~ 0.4 mm with a fill factor of 63.8%. Probe designs denoted by U and V achieve a compressed SS close to 4 µm with a WD of ~ 0 mm, with a fill factor of 66.5% and 96.4%, respectively. In order to achieve better agreement with ABCD predictions, the fill factor was limited to 63.7% [27], and the target l_{s1}, l_g lengths for the hybrid design were chosen to be 272 and 326 µm.

Ball lens-based probe results are shown in Fig. 5; (a) to (c) illustrate the various beam profiles that may be obtained and images of forward-viewing probes, while (d) to (f) present results from a side-viewing probe. Figure 5(a) shows the measured and ABCD predicted beam profiles for probes shown in Figs. 5(b) and 5(c) along with two other beam profiles, S and U. The inset shows the measured beam intensity profile of the probe marked V, in the xy plane, at a position close to the waist. The table in the figure again summarizes the lens segment lengths and the predicted WD and SS. A WD > 3.8 mm with an SS of 81 µm could be achieved using a 520 µm tip ball lens, shown in Fig. 5(c) (design V).

Figure 5(d) compares the beam profiles of a ~ 2.9 mm WD probe, before and after angle polishing. The insets show the beam intensity profiles of the forward- and side-viewing probes at a position close to the waist. The WD and SS for the side-viewing probe specified in the table were found by using a best-fit Gaussian to the measured beam profile. An image of the probe before angle polishing is shown in Figs. 5(e), and 5(f) depicts the same probe after angle polishing. The polishing angle was 48°, and the measured beam exit angle was $\beta = 6.37 \pm 0.3°$. The beam profiles before and after polishing matched closely, the WD for both the probes was ~ 2.9 mm, with an SS of ~ 72 µm. The beam intensity profiles, shown as insets in Fig. 5(d), also match, except for a slight astigmatism, visible on the side-viewing beam intensity profile.
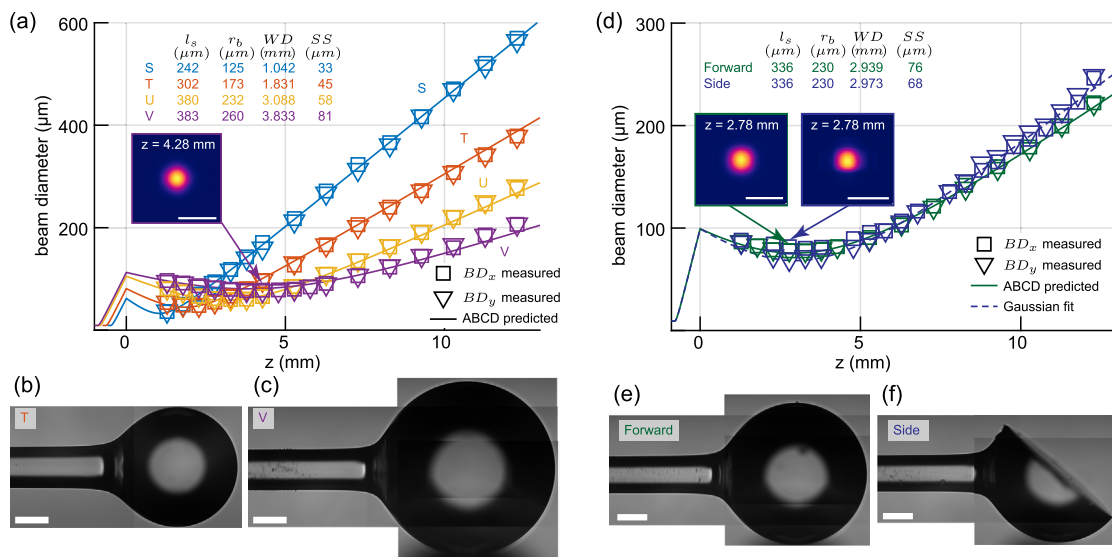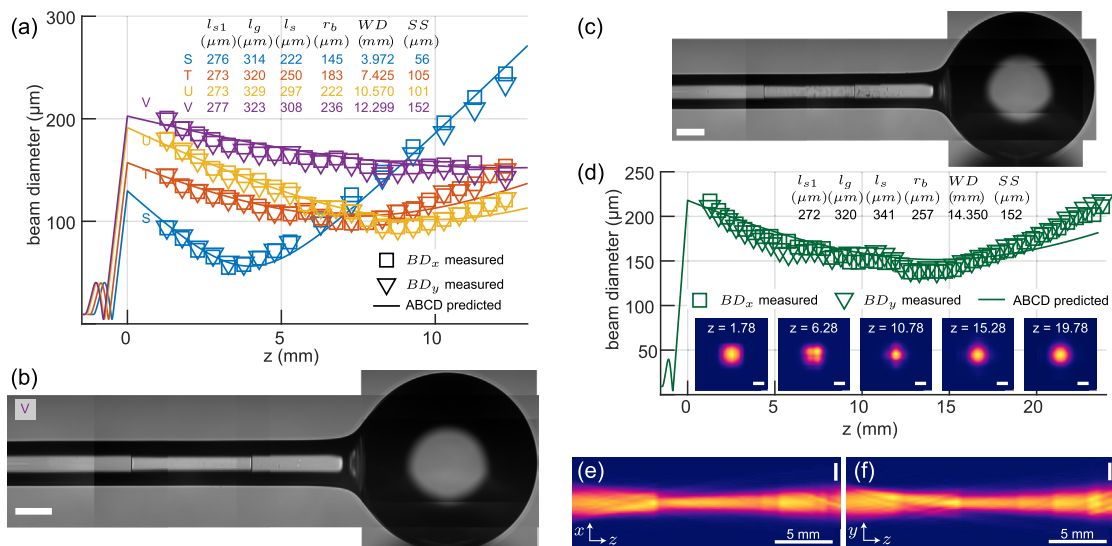

Fig. 5. Ball lens results. (a) Measured and predicted beam profiles for forward-viewing probes; (b) image of probe with a WD of ~ 1.8 mm and SS 45 µm, marked T; (c) image of probe with a 520 µm diameter ball tip, profile marked V; (d) comparison of beam profiles before and after angle polishing a 460 µm ball lens probe; (e) image of the forward-viewing probe, with profile shown in part (d); (f) image of the probe shown in part (e) after angle polishing at 48°; scale bars are 100 µm.

The increased WD and DoF enabled by the hybrid design are illustrated using results from forward-viewing hybrid probes in Fig. 6. Beam profiles shown in Fig. 6(a) demonstrate that a WD as large as ~ 3.97 mm may be achieved using a 290 µm diameter ball tip. Figure 6(b) shows the image of a hybrid probe with a 472 µm spherical tip that produces a roughly collimated beam with a WD of ~ 12.3 mm (marked as V). The group of results in Figs. 6(c)–6(f) illustrates the properties of a hybrid lens with a 14.35 mm WD and a ~ 27.9 mm DoF. The probe image is shown in Fig. 6(c), and the measured, predicted beam profiles are given in Fig. 6(d). The beam intensity profiles shown in the insets in Fig. 6(d) as well as in Figs. 6(e) and 6(f) show that a beam produced by this type of probe is approximately Gaussian in nature.

Figure 7 demonstrates the use of the hybrid lens for OCT imaging. This probe was designed to have a WD of ~ 6 mm, in order to obtain a roughly uniform BD over a 12 mm imaging range [23]. Figure 7(a) compares beam profiles of the forward-looking probe before angle polishing, the side-viewing probe after polishing and the side-viewing probe enclosed in the FEP sheath. In this case, the WD and the SS for the side-viewing probe (~ 5.75 mm and 48 µm, respectively), determined using the best-fit Gaussian, were identical to the forward-viewing profile. Figures 7(b) and 7(c) show images of the probes before and after angle polishing at 52°. The beam exit angle for the side-viewing probe was measured to be $\beta = 13.15 \pm 0.25°$. The beam intensity profiles for the forward- and side-viewing probes, at a position close to beam waist, are shown in Figs. 7(d) and 7(e).

When comparing the beam profiles of the side-viewing probe with and without the sheath, shown in Fig. 7(a), it can be seen that the beam characteristics in the x direction are approximately unchanged. However, the beam profile in the y direction is diverging and without a waist in the output medium. The astigmatic beam profile caused by the sheath is also illustrated by the beam intensity profile shown in Fig. 7(f).

OCT images acquired with the probe shown in Fig. 7(c), with and without a sheath, are shown in Figs. 7(g)–7(j). The loss of resolution caused by the use of a sheath is evident from a comparison of images Figs. 7(g) and 7(i). The impact of the sheath on images of the trachea is less clear; visually, Figs. 7(h) and (j) appear similar and seem to represent the airway shape and the underlying structures equally well.

5. DISCUSSION

The results obtained for the three types of all-fiber probes were consistent with the predictions obtained using the ABCD model and the Gaussian beam propagation method. The agreement between the ABCD predictions and the measured BDs for the GIF-based lenses was modest. It was found that a larger fill percentage of the GIF core and a longer GIF section were associated with a greater discrepancy between the predicted and measured results. The RMSE for plots S, T, U, and V were 19.7, 3.6, 61.1, and 231.9, respectively. Owing to these observations, the target CF and GIF dimensions for the hybrid lens were chosen to keep the fill factor less than $2/\pi$ [27]. For the ball lens designs shown in Fig. 5(a), the average RMSE between the measured and predicted BDs was 4.6 µm. For the hybrid lens results shown in Fig. 6(a), the average RMSE was 7.5 µm. Thus, the ABCD method was found to be adequately suited for the design of ball lens and hybrid lens probes.

The ball lensing procedure described here utilized a dedicated ball lensing system, as opposed to a fusion splicer used by previous studies [11–13,19,20,22]. This enabled the fabrication of larger spherical tips and consequently longer WD ball lens probes than have been reported. In the process described here, the ball tip is formed gradually using multiple arc discharges. Heat is transferred to the fiber tip by radiation and convection [29], and the molten glass naturally forms a sphere due to surface tension. The resulting spherical tips are highly symmetrical and produce nearly perfect Gaussian beam profiles, as illustrated in Fig. 5(a).
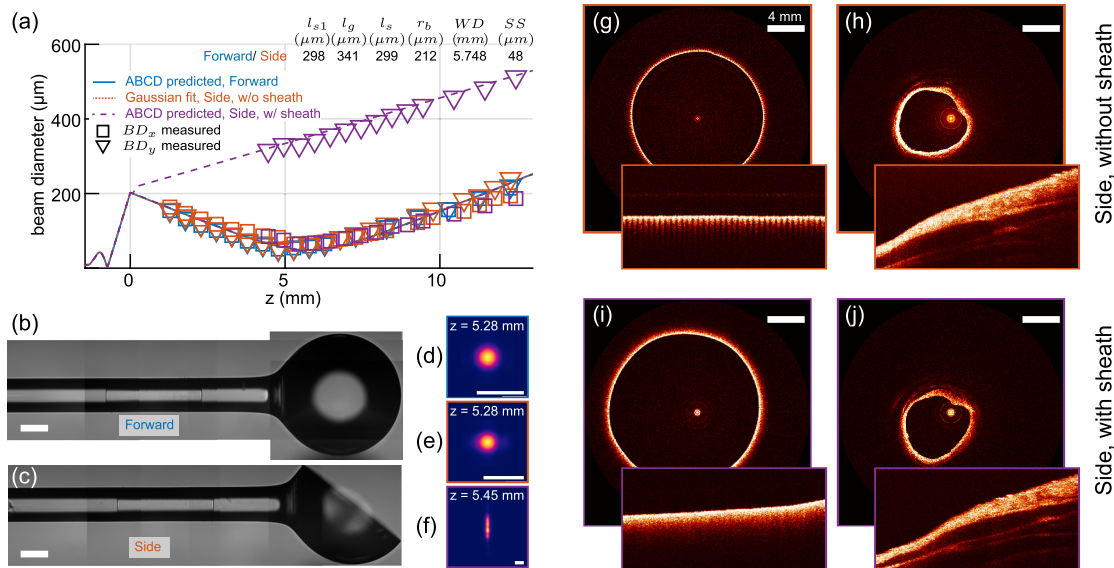

Fig. 6.   Forward-viewing hybrid lens probe results. (a) Measured and predicted beam profiles for four designs; (b) image of hybrid lens marked as V in (a); (c) image of 514 µm hybrid probe with 14.35 mm WD; (d) beam profiles for the probe shown in (c); the insets show beam intensity profiles at the z positions indicated in mm. (e), (f) Beam intensity profiles for the probe shown in (c) in the xz and yz planes; scale bars are 100 µm, unless noted.

Fig. 7. Side-viewing hybrid lens with ∼ 5.75 mm WD. (a) Measured and predicted beam profiles for the forward-viewing probe, side-viewing probe, and side-viewing probe enclosed in a sheath; (b), (c) images of the probe before and after angle polishing; (d), (e), (f) beam intensity profiles at a position close to the waist for the forward-viewing probe, side-viewing probe, and side-viewing probe enclosed in a sheath, respectively; (g), (h) OCT images acquired with the side-viewing probe in a rolled paper cylinder with 125 µm lines and an excised pig trachea, respectively; (i), (j) OCT images acquired with the side-viewing probe enclosed in a sheath of the same samples as (g) and (h); scale bars are 100 µm, unless noted.

The angle polishing process, presented in the Methods section, was robust and produced a single, well-defined beam by total internal reflection alone. As demonstrated in Figs. 5(d) and 7(a), the beam profiles, before and after angle polishing, matched closely. The measured beam exit angle was also consistent with predictions. However, the total internal reflection condition can be hampered by several factors, and this makes the angle-polishing process the most challenging aspect of the entire fabrication procedure. In order to ensure predictable results, care must be taken to ensure that the lens tip is clean, the polishing angle is correct, the extent of polish (i.e., the amount of spherical tip polished) is close to 50%, and that the polished surface is perfectly smooth. Any imperfection will result in multiple leaked beams or a grossly distorted main beam.

The results presented in Figs. 6 and 7 demonstrate that beams with significantly longer WDs may be produced with the hybrid lens design as compared to any other all-fiber design presented in the literature. The initial CF-GIF section produces a rapidly diverging beam within the second CF segment and allows better use of the limited aperture of the straight CF segment and the spherical tip. In the context of endoscopic OCT imaging, the use of a compound lens, with one segment employed to generate a compressed SS, was first demonstrated using bulk GRIN lenses and spacers by Fu *et al.* [30]. The hybrid lens presented here is an all-fiber realization of the same concept. The combination of a CF ball lens segment with a GIF section has also been proposed by Shiraishi *et al.* in the context of fiber-optic coupling [31]. Although the hybrid lens design utilizes some of the same elements, the principle of operation is different. Thus, the hybrid lens design approach presented here is novel, to the best of our knowledge.

As illustrated by Fig. 7, the sheath can dramatically alter the beam profile and decrease the image quality if not compensated

for. However, the pair of images shown in Figs. 7(h) and 7(j) indicate that the astigmatism produced by the sheath might not be very detrimental for the anatomical imaging of the large airways. Nevertheless, it is preferable to mitigate the impact of the sheath in order to improve resolution, and to reduce sensitivity roll-off over the imaging range. One approach to mitigate beam astigmatism is by the use of ellipsoidal ball lens designs [19,20,22]. While the ball-lensing procedure used here can only form spherical tips, the hybrid lens design can be used to obtain long WDs with relatively small tip sizes. Therefore, it should be feasible to fabricate low NA, long WD, hybrid probes with elliptical tips using a combination of the methods described here and the use of a fusion splicer to form the tip [19].

6. CONCLUSION

A novel, all-fiber lens design, suitable for endoscopic OCT imaging of the large airways, was demonstrated. This hybrid design achieves longer WDs and greater DoF than any other reported design thus far. Three all-fiber lens topologies were examined, and detailed modeling and fabrication notes for each type of design were also presented.

It is hoped that the details provided here will be of considerable help for designers of fiber-optic lenses, not only for endoscopic OCT imaging but also for fiber-optic coupling applications.

Disclosures. The authors declare no conflicts of interest.

Data Availability. All data that support the findings of this work are included within the paper.

Supplemental document. See Supplement 1 for supporting content.

REFERENCES

1. Z. Yaqoob, J. Wu, E. J. McDowell, X. Heng, and C. Yang, "Methods and application areas of endoscopic optical coherence tomography," J. Biomed. Opt. **11**, 063001 (2006).
2. M. J. Gora, M. J. Suter, G. J. Tearney, and X. Li, "Endoscopic optical coherence tomography: technologies and clinical applications," Biomed. Opt. Express **8**, 2405–2444 (2017).
3. S. Balakrishnan, R. Bu, C. M. Waters, B. M. Brandon, J. S. Kimbell, W. H. Stepp, W. W. Shockley, M. J. Clark, and A. L. Oldenburg, "Utility of endoscopic anatomical optical coherence tomography in functional rhinoplasty," J. Biomed. Opt. **25**, 016001 (2020).
4. J. J. Armstrong, M. Leigh, J. Walsh, D. Hillman, P. Eastwood, and D. Sampson, "Anatomical optical coherence tomography of the human upper airway," in *Optical Coherence Tomography: Technology and Applications*, W. Drexler and J. G. Fujimoto, eds. (Springer, 2008), pp. 1269–1291.
5. A. C. Loy, J. Jing, J. Zhang, Y. Wang, S. Elghobashi, Z. Chen, and B. J. Wong, "Anatomic optical coherence tomography of upper airways," in *Optical Coherence Tomography: Technology and Applications*, W. Drexler and J. G. Fujimoto, eds. (Springer, 2015), pp. 2245–2262.
6. G. K. Sharma, A. C. Loy, E. Su, J. Jing, Z. Chen, B. J. Wong, and S. Verma, "Quantitative evaluation of adult subglottic stenosis using intraoperative long-range optical coherence tomography," Ann. Otol. Rhinol. Laryngol. **125**, 815–822 (2016).
7. J. P. Williamson, R. A. McLaughlin, M. J. Phillips, A. Curatolo, J. J. Armstrong, K. J. Maddison, R. E. Sheehan, D. D. Sampson, D. R. Hillman, and P. R. Eastwood, "Feasibility of applying real-time optical imaging during bronchoscopic interventions for central airway obstruction," J. Bronchol. Interventional Pulmonol. **17**, 307–316 (2010).
8. G. J. Tearney, "Optical biopsy of in vivo tissue using optical coherence tomography," Ph.D. dissertation (Massachusetts Institute of Technology, 1996).
9. J. C. Jing, "Visualization of the upper airway health using optical coherence tomography," Ph.D. dissertation (University of California at Irvine, 2016).
10. X. Sun and J. Li, "Design of a long working distance graded index fiber lens with a low NA for fiber-optic probe in OCT application," Proc. SPIE **8938**, 89380B (2014).
11. M. Shishkov, G. Tearney, and B. Bouma, "Sculptured optical fiber tips for narrow diameter optical catheters," in *Biomedical Topical Meeting* (Optical Society of America, 2004), paper SE5.
12. V. X. Yang, Y. X. Mao, N. Munce, B. Standish, W. Kucharczyk, N. E. Marcon, B. C. Wilson, and I. A. Vitkin, "Interstitial Doppler optical coherence tomography," Opt. Lett. **30**, 1791–1793 (2005).
13. Y. Mao, S. Chang, and C. Flueraru, "Fiber lenses for ultra-small probes used in optical coherent tomography," J. Biomed. Sci. Eng. **3**, 27–34 (2010).
14. E. Swanson, C. L. Petersen, E. McNamara, R. B. Lamport, and D. L. Kelly, "Ultra-small optical probes, imaging optics, and methods for using same," U.S. patent 6,445,939 (3 September 2002).
15. H. Li, B. A. Standish, A. Mariampillai, N. R. Munce, Y. Mao, S. Chiu, N. E. Marcon, B. C. Wilson, A. Vitkin, and V. X. Yang, "Feasibility of inter-

stitial Doppler optical coherence tomography for in vivo detection of microvascular changes during photodynamic therapy," Lasers Surg. Med. **38**, 754–761 (2006).
16. Y. Mao, S. Chang, S. Sherif, and C. Flueraru, "Graded-index fiber lens proposed for ultrasmall probes used in biomedical imaging," Appl. Opt. **46**, 5887–5894 (2007).
17. S. Y. Ryu, H. Y. Choi, J. Na, W. J. Choi, and B. H. Lee, "Lensed fiber probes designed as an alternative to bulk probes in optical coherence tomography," Appl. Opt. **47**, 1510–1516 (2008).
18. D. Lorenser, X. Yang, and D. D. Sampson, "Ultrathin fiber probes with extended depth of focus for optical coherence tomography," Opt. Lett. **37**, 1616–1618 (2012).
19. W. Yuan, R. Brown, W. Mitzner, L. Yarmus, and X. Li, "Super-achromatic monolithic microprobe for ultrahigh-resolution endoscopic optical coherence tomography at 800 nm," Nat. Commun. **8**, 1531 (2017).
20. H. S. Cho, S.-J. Jang, K. Kim, A. V. Dan-Chin-Yu, M. Shishkov, B. E. Bouma, and W.-Y. Oh, "High frame-rate intravascular optical frequency-domain imaging in vivo," Biomed. Opt. Express **5**, 223–232 (2014).
21. Y. Wu, J. Xi, L. Huo, J. Padvorac, E. J. Shin, S. A. Giday, A. M. Lennon, M. I. F. Canto, J. H. Hwang, and X. Li, "Robust high-resolution fine OCT needle for side-viewing interstitial tissue imaging," IEEE J. Sel. Top. Quantum Electron. **16**, 863–869 (2009).
22. K. Tan, M. Shishkov, A. Chee, M. Applegate, B. Bouma, and M. Suter, "Flexible transbronchial optical frequency domain imaging smart needle for biopsy guidance," Biomed. Opt. Express **3**, 1947–1954 (2012).
23. S. Balakrishnan, R. Bu, N. Iftimia, H. Price, C. Zdanski, and A. L. Oldenburg, "Combined anatomical optical coherence tomography and intraluminal pressure reveal viscoelasticity of the in vivo airway," J. Biomed. Opt. **23**, 100501 (2018).
24. W. Emkey and C. Jack, "Analysis and evaluation of graded-index fiber lenses," J. Lightwave Technol. **5**, 1156–1164 (1987).
25. W. Jung, W. A. Benalcazar, A. Ahmad, U. Sharma, H. Tu, and S. A. Boppart, "Numerical analysis of gradient index lens-based optical coherence tomography imaging probes," J. Biomed. Opt. **15**, 066027 (2010).
26. C. Duan, J. Sun, S. Samuelson, and H. Xie, "Probe alignment and design issues of microelectromechanical system based optical coherence tomography endoscopic imaging," Appl. Opt. **52**, 6589–6598 (2013).
27. D. Lorenser, X. Yang, and D. D. Sampson, "Accurate modeling and design of graded-index fiber probes for optical coherence tomography using the beam propagation method," IEEE Photon. J. **5**, 3900015 (2013).
28. S. Balakrishnan, "Endoscopic optical coherence tomography imaging of the airway," Ph.D. dissertation (University of North Carolina at Chapel Hill, 2021).
29. R. Wiley and B. Clark, "Large area isothermic plasma for large diameter and specialty fiber splicing," in *OFC/NFOEC* (IEEE, 2008), pp. 1–3.
30. H. L. Fu, Y. Leng, M. J. Cobb, K. Hsu, J. H. Hwang, and X. Li, "Flexible miniature compound lens design for high-resolution optical coherence tomography balloon imaging catheter," J. Biomed. Opt. **13**, 060502 (2008).
31. K. Shiraishi, H. Ohnuki, N. Hiraguri, K. Matsumura, I. Ohishi, H. Morichi, and H. Kazami, "A lensed-fiber coupling scheme utilizing a graded-index fiber and a hemispherically ended coreless fiber tip," J. Lightwave Technol. **15**, 356–363 (1997).